remote sensing

MDPI

Article

The Influence of Spatial Scale Effect on Rock Spectral Reflectance: A Case Study of Huangshan Copper–Nickel Ore District

Ziwei Wang [1,†], Huijie Zhao [1,2,†], Guorui Jia [1,*] and Feixiang Wang [1]

[1] Ministry of Education Key Laboratory of Precision Opto-Mechatronics Technology, School of Instrumentation and Optoelectronic Engineering, Beihang University, Beijing 100191, China; ziweiwang@buaa.edu.cn (Z.W.); hjzhao@buaa.edu.cn (H.Z.); fxwang@buaa.edu.cn (F.W.)

[2] Key Laboratory of Ministry of Industry and Information Technology, Institute of Artificial Intelligence, Aerospace Optical-Microwave Integrated Precision Intelligent Sensing, Beihang University, Beijing 100191, China

* Correspondence: jiaguorui@buaa.edu.cn

† These authors contributed equally to this work.

Abstract: The spectral reflectance measured in situ is often regarded as the "truth". However, its limited coverage and large spatial heterogeneity often make the ground-based reflectance unable to represent the remote sensing images. Since the spatial scale mismatch between ground-based, airborne, and spaceborne measurements, the applications of geological exploration, metallogenic prognosis and mine monitoring are facing severe challenges. In order to explore the influence of spatial scale effect on rock spectra, spectral reflectance with uncertainty caused by differences in illumination view geometry and spatial heterogeneity is introduced into the Bayesian Maximum Entropy (BME) method. Then, the rock spectra are upscaled from the point-scale to meter-scale and to 10 m-scale, respectively. Finally, the influence of spatial scale effect is evaluated based on the reflectance value, spectral shape, and spectral characteristic parameters. The results indicate that the BME model shows better upscaling accuracy and stability than Ordinary Kriging and Ordinary Least Squares model. The maximum Euclidean Distance of rock spectra caused by spatial resolution change is 6.271, and the Spectral Angle Mapper can reach 0.370. The spectral absorption position, absorption depth, and spectral absorption index are less affected by scale effect. For the area with similar spatial heterogeneity to the Huangshan Copper–Nickel Ore District, when the spatial resolution of the image is greater than 10 m, the rock's spectrum is less influenced by the change in spatial resolution. Otherwise, the influence of spatial scale effect should be considered in applications. In addition, this work puts forward a set of processes to evaluate the influence of spatial scale effect in the study area and carry out the upscaling.

Keywords: rock's spectral reflectance; spatial scale effect; spatial heterogeneity; upscaling model; Bayesian Maximum Entropy; spectral characteristics; spectral fluctuation

check for updates

Citation: Wang, Z.; Zhao, H.; Jia, G.; Wang, F. The Influence of Spatial Scale Effect on Rock Spectral Reflectance: A Case Study of Huangshan Copper–Nickel Ore District. *Remote Sens.* **2024**, *16*, 4643. https://doi.org/10.3390/rs16244643

Academic Editor: Akira Iwasaki

Received: 3 November 2024
Revised: 4 December 2024
Accepted: 10 December 2024
Published: 11 December 2024

Copyright: © 2024 by the authors. Licensee MDPI, Basel, Switzerland. This article is an open access article distributed under the terms and conditions of the Creative Commons Attribution (CC BY) license (https://creativecommons.org/licenses/by/4.0/).

1. Introduction

In situ measurements are usually regarded as the primary source for the relative truth of the objects. It plays an important role in the vicarious calibration, atmospheric correction, remote sensing product validation, and object identification [1–5]. However, the footprint coverage of in situ measurements is limited. It is smaller than the spatial resolution of remote sensing images. Moreover, because of the spatial heterogeneity of most land surfaces, the in situ measurements usually cannot represent the remote sensing images [6–8]. The spatial scale mismatch and the surface heterogeneity lead to spatial scale effects among ground-based, airborne, and spaceborne measurements.

For more than 60 years, researchers have realized the importance of scale in the spatial organization of human activities and the physical processes on the Earth's surface [9]. Ignoring the spatial scale effect will affect the estimation accuracy of albedo, the prediction of rainfall-runoff and the inversion accuracy of surface parameters [10,11]. The spectrum

fluctuation caused by the spatial scale effects makes the metallogenic prognosis, resource management, and environmental monitoring severely challenging [12]. Therefore, the transfer of information from one scale to another and the influence of spatial scale effect have become research focuses [9]. Previous studies have shown that the spatial heterogeneity of the land surfaces, the nonlinearity of the retrieval algorithm, and the nonlinearity of the spatial response function are regarded as the three main reasons for the spatial scale effect [13–15]. Spatial heterogeneity is considered to be the fundamental reason for this, because an entirely homogeneous land surface does not exist [16–18].

Upscaling is an effective way of solving the spatial scale mismatch, which refers to converting high-resolution information into low-resolution [10]. Upscaling methods mainly include the arithmetic average method, empirical regression method, geostatistics method, and Bayesian method. The upscaling accuracy of the arithmetic average methods depends on the distribution of sampling points and the spatial heterogeneity of pixels [19–21]. The empirical regression method depends on the reliability of historical data, and the robustness of empirical relationships is lower [22,23]. Moreover, it does not consider the spatio-temporal distribution and spatial autocorrelation of surface parameters. The Kriging method, based on geostatistics, introduces spatial structure information. However, it requires the surface parameters conform to normal distribution and second-order stationarity assumptions [24–26].

Based on geostatistical techniques, the Bayesian Maximum Entropy (BME) method is proposed. It is a nonlinear estimator which is suitable for estimating the surface parameters with strong spatial heterogeneity and non-normal distribution [27]. The BME method divides data into hard data and soft data according to their accuracy. Hard data refers to data that are accurate enough or where the error is minimal, while soft data refers to data that are relatively inaccurate [28]. This method can introduce uncertainty data into estimation, which provide an important tool for solving spatial scale problems. The BME method has been successfully applied in the upscaling process of parameters such as ozone, particle matter 10, soil moisture content, and leaf area index [29–32]. It is worth noting that previous studies usually use a single model prediction value as soft data. However, the prediction value under different conditions is often a fluctuation range.

The BME method has achieved good results in upscaling. However, in rock-related applications, spectrum measured in situ are still used as reference spectrum to directly participate in the applications [33–36]. At present, the rock's spectrum inconsistency between in situ measurement and the images caused by spatial scale effects has aroused widespread concern. Previous studies have used the method of continuous removal to normalize the absorption characteristics of rock spectrum to a consistent spectral background, to suppress the influence of background spectrum, and to highlight the spectral characteristics [37,38]. However, the influence of the spatial scaling effect has not been fundamentally eliminated. Because the upscaling methods are rarely used to convert the spectral reflectance of rocks measured in situ into pixel scale. The influence of spatial scale effects on reflectance value, spectral shape, and absorption characteristics of rocks has not been studied in detail.

This work puts forward a set of processes for evaluating the influence of spatial scale effect on the spectral reflectance of rocks in the study area. One of the innovative aspects of this work is to introduce two kinds of uncertainty data as soft data to construct the BME upscaling model. Then, compared with the Ordinary Least Squares model and the Ordinary Kriging model which only uses hard data, the advantages of the BME upscaling model after introducing uncertainty data as soft data are verified and evaluated. After that, based on the BME upscaling model, the spectral reflectance of rocks is upscaled from point-scale to pixel-scale with the spatial resolutions of 1 m, 2 m, 3 m, 5 m, 10 m, 30 m, and 50 m, respectively. Finally, this work quantitatively evaluates the influence of spatial scale effect on the spectral reflectance of rocks based on three aspects: reflectance value, spectral shape, and spectral absorption characteristics.

2. Materials and Methodology

2.1. Study Area

The Huangshan Copper–Nickel Ore District is located about 125 km southeast of Hami City, Xinjiang Uygur Autonomous Region, China. The terrain of this area mainly includes low hills with a relative elevation of 10–50 m. The Ore district belongs to the desert Gobi landscape area, which is characterized by perennial dryness, less air pollution, and weak atmospheric scattering and water vapor absorption. Moreover, the vegetation coverage is scarce, and the rocks are primarily physically weathering. Therefore, the spatial heterogeneity of this area experienced little change over time.

In addition, the Huangshan Copper–Nickel Ore District is rich in mineral resources, complete in rock types, and exposed from bedrock to intermediate-acid rocks, which is very suitable for the upscaling study of rock spectral reflectance. There are many kinds of metal minerals in the ore district, such as gold, copper, and nickel. Host-rock alteration mainly includes Pyritization, Limonitization, Chloritization, Chalcopyritization, Malachitization, and Carbonatization [39]. Therefore, the Huangshan Copper–Nickel Ore District was selected as the study area, as shown in Figure 1. Its geographical range is between 94.588°E–94.616°E and 42.257°N–42.269°N, with an area of 3.7 km × 1.3 km.

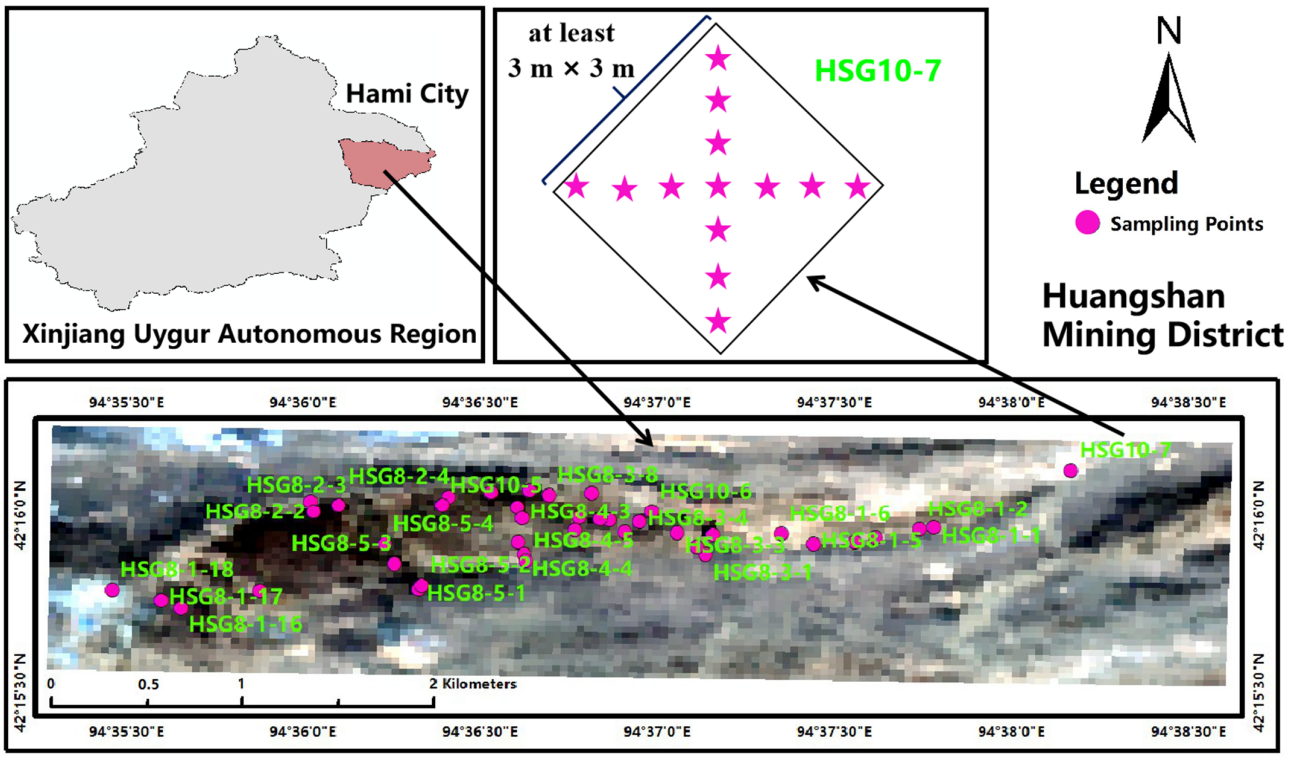

Figure 1. Overview of the study area and the 40 ground sample points. The bottom image is the Hymap hyperspectral image covering the study area on 22 October 2002.

2.2. In Situ Measurements Data

There are 40 ground sampling points in the study area which are evenly laid out in the Huangshan Copper–Nickel Ore District according to the size, shape, and rock type of the mineral deposit. In order to evaluate the spatial heterogeneity around each sampling point, the spectral reflectance of 40 ground sampling points were collected at noon local time. In addition to collecting the spectra in the center of each sampling point, the spectra were collected at intervals in four directions at intervals of approximately 50 cm. The spectra of 13 locations were collected around each sampling point, covering an area of at least 3 m × 3 m (Figure 1). During the in situ measurements, the environmental conditions were

recorded, including the date, time, latitude and longitude, illumination view geometry, and cloud cover, etc.

At each location, 7 measurements were made on the reference panel and the rock surface. The measurement sequence was firstly the panel, then the rock surface 5 times, and the panel once more. Each individual measurement consisted of 5 scans, therefore, a total of 25 rock spectral reflectances were generated for each location. The arithmetic average of 25 spectra were taken as the in situ measured spectral reflectance at this location. This procedure used two major apparatus to collect the spectral reflectance: an Analytical Spectroscopy Device (ASD) FieldSpec Pro spectrometer (Analytical Spectral Devices CO., Inc., Boulder, CO, USA) and a Spectralon standard panel (Labsphere, Inc., North Sutton, NH, USA). The ASD FieldSpec Pro spectrometer is equipped with a 25° fore optic lens, covering the spectral range of 350–2500 nm. It has a spectral resolution of 3 nm and 10 nm in the VNIR spectral regions and the SWIR spectral regions [40]. The 99% reflectance Spectralon® standard panel was used as a reference panel to acquire the reflectance factor.

2.3. Bayesian Maximum Entropy (BME) Method

The BME is based on the spatiotemporal random field (STRF), which is a theoretical framework for studying the phenomena and natural processes evolving in the spatial and/or temporal continuum. In the STRF theory, the metallogenic process is a natural process that evolves in time and space, which can be expressed as a STRF specified by the variable $X(p)$. The vector $P = [P_1 \dots P_m]$ represents the point positions in space-time, where each position $P_i = (s_i, t_i)$, $i = 1, \dots, m$, consists of space coordinates s_i and time coordinates t_i. Therefore, the vector $\chi = [\chi_1, \dots, \chi_m]$ indicates a set of sampled or simulated values of the random variables $x = [x_1, \dots, x_m]$ at space and time point locations $P = [P_1 \dots P_m]$ [41].

The BME method is a spatio-temporal mapping method based on maximum entropy theory and Bayesian law, which makes it possible to logically incorporate the measured values with various knowledge bases [42–44]. In this work, spectral reflectance measured in situ at the center of each sampling point were used as hard data. The measured reflectance with uncertainty caused by differences in illumination view geometry and spatial heterogeneity were used as soft data.

The BME method is usually divided into three stages: a prior stage, a meta-prior stage and a posterior stage. The purpose of the prior stage is to calculate the prior probability distribution function (PDF) based on the maximum entropy theory when Equation (1) reaches the maximum value. According to the Shannon information theory, the expression for the entropy function of the prior PDF is as follows:

$$H(f_G(\chi_{map})) = E[Info_G(f_G(\chi_{map}))] = -\int f_G(\chi_{map}) \log f_G(\chi_{map}) d\chi_{map} \quad (1)$$

where $f_G(\chi_{map})$ is the prior PDF, G refers to the general knowledge, and χ_{map} consists of a vector of points, which can be expressed as follows:

$$\chi_{map} = [\chi_{hard}, \chi_{soft}, \chi_k], \quad (2)$$

where χ_{hard} and χ_{soft} refer to the hard data and soft data; χ_k is the value of the position to be upscaled. The constraint condition that Equation (1) reaches the maximum value can be expressed as:

$$E(g_a) = \int g_a(\chi_{map}) f_G(\chi_{map}) d\chi_{map} \; a = 0, \cdots, N_c. \quad (3)$$

Here, $E(g_a)$ refers to the expected value of the constraint condition; $g_a(\chi_{map})$ is a set of functions of χ_{map}, such as the normalization, expectation, variance, and covariance; N_c refers to the total number of constraint conditions. Based on the Lagrangian multiplier μ_a,

the expression $f_G(\chi_{map})$ can be obtained by finding the maximum value of Equation (4) under the constraint conditions.

$$\begin{aligned} L(f_G(\chi_{map})) &= -\int f_G(\chi_{map}) \log f_G(\chi_{map}) d\chi_{map} \\ &\quad - \sum_{a=0}^{N_C} \mu_a [\int g_a(\chi_{map}) f_G(\chi_{map}) d\chi_{map} - E[g_a(\chi_{map})]] \end{aligned} \tag{4}$$

then, the prior PDF $f_G(\chi_{map})$ can be described as:

$$f_G(\chi_{map}) = \frac{1}{A} \exp(\sum_{a=1}^{N_c} \mu_a g_a(\chi_{map})), \tag{5}$$

where $A = \int \exp(\sum_{a=1}^{N_c} \mu_a g_a(\chi_{map})) d\chi_{map}$, which is used to normalize $f_G(\chi_{map})$.

The task of the meta-prior stage is to express soft data in the most appropriate way. Common soft data expressions include interval type, probability type, and function type. In the posterior stage, the posterior PDF can be obtained based on the prior PDF and the formulation of Bayesian law.

$$f_K(\chi_k) = f_G(\chi_k | \chi_{hard}, \chi_{soft}) = \frac{f_G(\chi_k, \chi_{hard}, \chi_{soft})}{f_G(\chi_{hard}, \chi_{soft})}. \tag{6}$$

Here, $f_K(\chi_k)$ refers to the posterior PDF; K refers to all the data used in this work.

2.4. Ordinary Kriging (OK) Method

In fact, if the variogram is used as the prior knowledge in the BME method, only hard data are used to calculate the posterior PDF in the meta-prior stage and posterior stage, without introducing soft data, and the maximum posterior probability is taken as the final upscaling results. Under this condition, the expression of the BME upscaling model is equivalent to the upscaling model constructed using the OK method [28,45]. Therefore, this study is based on the OK method to verify the upscaling ability of the BME model constructed in this paper and the advantages of introducing soft data.

The OK is an optimal linear unbiased estimation method, which can be expressed as:

$$Z^*(x_o) = \sum_{i=1}^{n} \lambda_i Z(x_i). \tag{7}$$

Here, $Z^*(x_o)$ refers to the upscaling result of point x_o to be estimated; $Z(x_i)$ is the in situ measured spectral reflectance at the sample point x_i; n is the number of sample points; λ_i refers to the weight coefficient. To ensure optimal linear unbiased estimation, the variance between $Z^*(x_o)$ and $Z(x_o)$ needs to be minimized, and the constraint condition needs to satisfy Equation (8).

$$\sum_{i=1}^{n} \lambda_i = 1 \tag{8}$$

Based on Lagrange Multiplier method, the weight coefficient λ_i can be calculated using Equation (9):

$$\lambda = C^{-1} \times c_0. \tag{9}$$

Here, C refers to the matrix of the covariances; c_0 refers to the vector at which the covariances was estimated. A function of the separated distance can be calculated using the variogram:

$$C(h) = c_{nugget} + c_{sill} - \gamma(h). \tag{10}$$

Here, c_{nugget} and c_{sill} refer to the nugget and the partial sill; h represents the spatial distance between any two sampling points. $\gamma(h)$ is the semivariogram, which can be calculated using the semi-variance function:

$$\gamma(h) = \frac{1}{2N(h)} \sum_{i=1}^{N(h)} (x_i - x_{i+h})^2, \tag{11}$$

where $N(h)$ represents the number of pair of points x_i and x_{i+h} for the given distance h. In the work, the exponential model was used to describe the variogram, which can be described as:

$$\gamma(h) = c_{nugget} + c_{sill}(1 - e^{\frac{3h}{a}}), \tag{12}$$

where a refers to the lag distance that stands for the correlation length.

2.5. Evaluating Indicator

The Spectral Angle Mapper (SAM), the Euclidean distance (ED), and the standard deviation (STD) are used to evaluate the spatial heterogeneity of each sampling point. The SAM is used to evaluate the spectral shape similarity between the two spectra, while the ED is used to evaluate the distance between the two spectra [46]. The STD is used to reflect the dispersion of the spectral data set collected around each sampling point. The smaller the SAM, ED, and STD, the smaller the spatial heterogeneity of sampling points.

$$SAM = \frac{\widehat{y}_i^T y_i}{(\left\| \widehat{y}_i \right\|)(\| y_i \|)} = \frac{\widehat{y}_i^T y_i}{\sqrt{y_i^T y_i}\sqrt{\widehat{y}_i^T \widehat{y}_i}}, \tag{13}$$

$$ED = \sqrt{\sum_{i=1}^{n} (y_i - \hat{y}_i)^2}, \tag{14}$$

$$STD = \sqrt{\frac{1}{n} \sum_{i=1}^{n} (y_i - \hat{y}_i)^2}, \tag{15}$$

where y_i refers to the spectral reflectance measured in situ; $\widehat{y}_i$ is the upscaled spectral reflectance; $\overline{y}_i$ is the mean value; n is the number of bands.

Since there are 40 ground sampling points in the study area, the sample size of the data set is small. Therefore, this study uses the Leave-One-Out (LOO) method to cross-verify the ability of the upscaling model. Four indicators were used to quantitatively evaluate the accuracy of upscaling results: the Mean Absolute Error (MAE), the Root Mean Square Error (RMSE), the SAM, and the coefficient of determination (R^2). MAE and RMSE are used to measure the closeness between the two spectra. The smaller the MAE, RMSE, and SAM, the better the upscaling ability of the model. R^2 is usually used to measure the goodness of fit of the model. The closer R^2 is to 1, the better the fitting effect of the constructed model.

$$MAE = \frac{1}{n} \sum_{i=1}^{n} (|y_i - \hat{y}_i|) \tag{16}$$

$$RMSE = \sqrt{\frac{1}{n} \sum_{i=1}^{n} (y_i - \hat{y}_i)^2} \tag{17}$$

$$R^2 = 1 - \frac{\sum_{i=1}^{n} (y_i - \hat{y}_i)^2}{\sum_{i=1}^{n} (y_i - \overline{y}_i)^2} \tag{18}$$

3. Results

3.1. Spatial Autocorrelation of Study Area

Based on the semivariogram and exponential model (Equations (11) and (12)), the spatial autocorrelation of the whole study area is evaluated and analyzed. Figure 2 shows the semivariogram of rock spectral reflectance in four representative bands in the study area. The semivariogram is used to describe the variation in rock spectral reflectance at different distances. According to Tobler's First Law of Geography, the semivariogram will increase with the increase in distance, and the spatial autocorrelation between sampling points will be smaller. When the semivariogram no longer increases with the increase in distance, it shows that the region no longer has spatial autocorrelation. As can be seen from Figure 2, for the four representative bands, when the lag distance is increased to about 3773.62 m, the semivariogram reaches equilibrium. This shows that the rock spectral reflectance in the area of 3773.62 m × 3773.62 m has strong spatial autocorrelation. The spatial autocorrelation of the study area is the research basis of geostatistics. Therefore, within the area of 3.7 km × 1.3 km selected in this work, this study has a certain theoretical basis and research significance for studying the upscaling of rock spectrum and analyzing the influence of spatial scale effect using geostatistics.

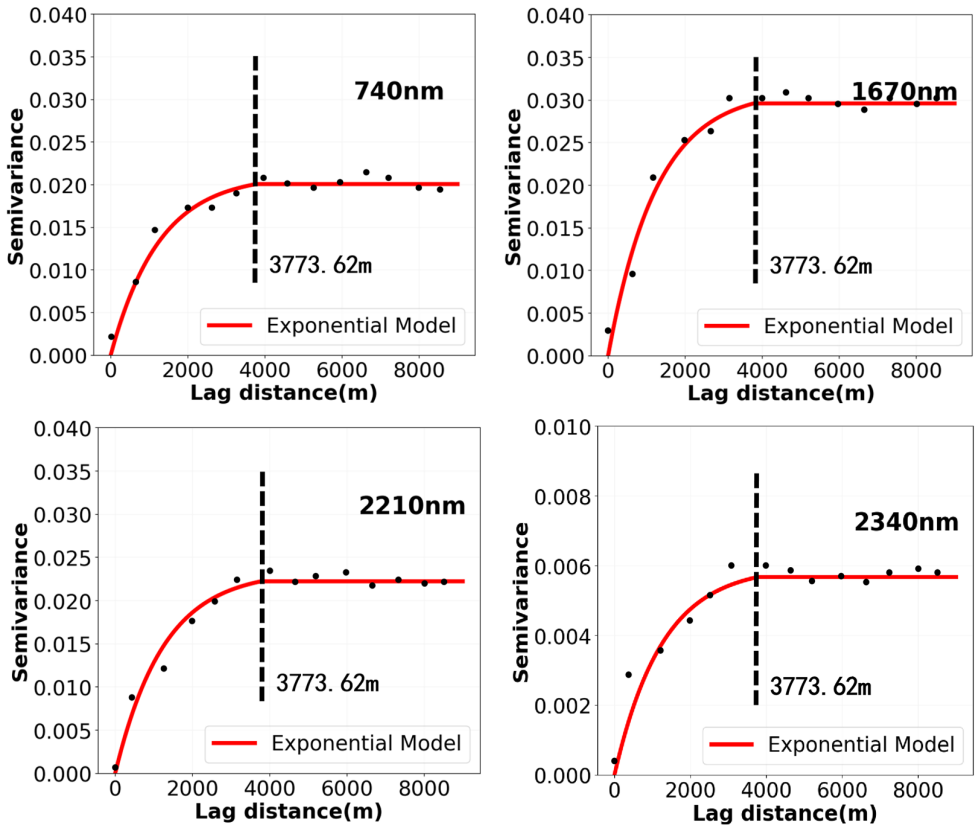

Figure 2. Semivariogram of representative bands of spectral reflectance measured in situ in the study area.

3.2. Spatial Heterogeneity of Sampling Points

The spatial heterogeneity of each sampling point is evaluated using the SAM, ED, and STD between the in situ measured spectral reflectance collected at 13 locations around each sampling point, and the calculation results are shown in Table 1. Comparing the spatial heterogeneity of 40 sampling points, the differences in the SAM, ED, and SD between different sampling points can reach 0.097, 5.230, and 0.107, respectively. This shows that the spatial heterogeneity of different sampling points in the study area is quite different, which is suitable for evaluating the upscaling ability of the model and analyzing the influence of

spatial heterogeneity on scale effect. In addition, these calculation results will be used as soft data, and to study the influence of spatial scale effect on the rock's spectral reflectance in the following section.

Table 1. Spatial heterogeneity of 40 sampling points in the Huangshan Copper–Nickel Ore District.

Sampling Point	SAM	ED	STD	Sampling Point	SAM	ED	STD
HSG10-5	0.067	1.383	0.051	HSG8-2-5	0.021	1.045	0.032
HSG10-6	0.031	1.834	0.098	HSG8-2-6	0.046	0.887	0.061
HSG10-7	0.043	0.575	0.016	HSG8-3-1	0.053	0.965	0.011
HSG8-1-1	0.031	2.269	0.054	HSG8-3-2	0.090	1.216	0.055
HSG8-1-15	0.040	0.484	0.006	HSG8-3-3	0.038	5.714	0.113
HSG8-1-16	0.036	0.803	0.012	HSG8-3-4	0.086	0.988	0.010
HSG8-1-17	0.024	1.702	0.069	HSG8-3-5	0.070	1.755	0.056
HSG8-1-18	0.118	3.303	0.060	HSG8-3-6	0.054	1.007	0.009
HSG8-1-2	0.075	2.707	0.064	HSG8-3-7	0.040	1.477	0.056
HSG8-1-3	0.060	2.542	0.071	HSG8-3-8	0.053	1.502	0.051
HSG8-1-4	0.037	2.220	0.044	HSG8-3-9	0.038	2.045	0.055
HSG8-1-5	0.063	1.535	0.054	HSG8-4-1	0.031	1.371	0.063
HSG8-1-6	0.023	1.479	0.065	HSG8-4-2	0.038	2.655	0.067
HSG8-1-7	0.049	0.859	0.009	HSG8-4-3	0.039	2.846	0.079
HSG8-1-8	0.048	1.476	0.013	HSG8-4-4	0.023	1.415	0.065
HSG8-1-9	0.059	1.268	0.025	HSG8-4-5	0.057	0.918	0.053
HSG8-2-1	0.054	4.161	0.070	HSG8-5-1	0.039	1.183	0.009
HSG8-2-2	0.060	1.020	0.022	HSG8-5-2	0.031	3.207	0.038
HSG8-2-3	0.043	1.557	0.017	HSG8-5-3	0.037	0.690	0.026
HSG8-2-4	0.035	4.816	0.083	HSG8-5-4	0.073	2.159	0.051

3.3. Soft Data

Because in situ measurements are usually vertical observations, and the remote sensing image will also be corrected to the nadir view through the atmospheric correction process. Meanwhile, the influence of different view azimuth angles can be ignored when the view zenith angles of in situ measured and image data are both 0°. Therefore, in this study, the uncertainty data caused by the inconsistency of solar zenith angles (SZA) and solar azimuth angles (SAA) between in situ measured and image pixel-scale spectral reflectance are regarded as the first type of interval soft data.

In order to ensure sufficient solar radiation intensity, the measurement time of the sun-synchronous orbit satellite and in situ measurements are usually between 10:00 and 14:00 local time. In addition, the SZA of the Huangshan Copper–Nickel Ore District is large in winter, and it is often covered by snow. Therefore, in situ measurements in this area are usually not carried out in winter. In this work, the variation range of SZA and SAA in this area from March to October in 2010–2024 was calculated at 10:00–14:00 local time. According to the statistical results, the variation range of SZA and SAA is around 19°–67° and 122°–248°.

Therefore, based on previous experimental research [47], the uncertainty data of rock spectral reflectance at 40 ground sampling points was calculated, when the range variation in SZA and SAA was from 20° to 70° and 120° to 250°. The formula for calculating the uncertainty of in situ measured spectral reflectance caused by the inconsistency of SZA and SAA in this study is as follows:

$$\sigma = k \times \sqrt{(U_{SZA})^2 + (U_{SAA})^2 + 2U_{SZA}U_{SAA}r(x_{SZA}, x_{SAA})}. \quad (19)$$

Here, U_{SZA} and U_{SAA} refer to the uncertainty caused by the inconsistency of SZA and SAA, respectively; $r(x_{SZA}, x_{SAA})$ refers to the correlation coefficients; k is the coverage factor, which is taken as 2 in this work.

Based on the calculation results of Equation (19), the possible fluctuation range of spectral reflectance measured in situ caused by the inconsistency of SZA and SAA can be estimated by using the following formula:

$$l_{ij} = R_{ij} - \sigma_{ij}, \tag{20}$$

$$v_{ij} = R_{ij} + \sigma_{ij}. \tag{21}$$

Here, l_{ij} and v_{ij} are the possible lower and upper bounds of spectral reflectance at sampling point i in band j; R_{ij} refers to the spectral reflectance measured in situ; σ_{ij} is the uncertainty caused by different SZA and SAA. By using Equations (19)–(21), an interval statement was used to describe the first type uncertainty data, as can be expressed as:

$$\chi_{soft_1} = \left\{ [\chi_{1j} \cdots \chi_{ij}]^T; \chi_{ij} \in [l_{ij}, v_{ij}], i = 1 \ldots 40, j = 1 \ldots 2151 \right\}, \tag{22}$$

where χ_{ij} is the soft data of the band j at the sampling point i. Figure 3 shows the fluctuation interval of spectral reflectance measured in situ that may be caused by different SZA and SAA at partial sampling points.

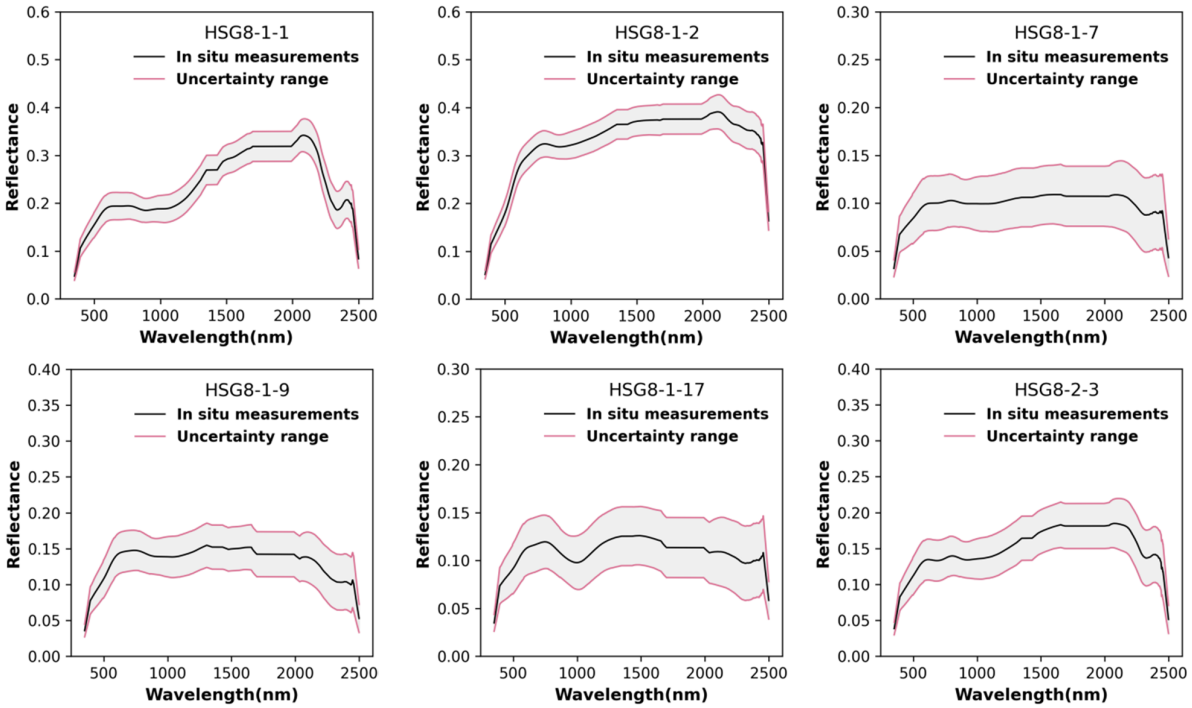

Figure 3. The fluctuation interval in the in situ measured spectral reflectance of rocks when the SZA and SAA is inconsistent with the image data, at some sampling points.

In addition, the uncertainty data caused by spatial heterogeneity around the sample point can be expressed by uniformly collecting spectra from multiple locations around the sample point and calculating their STD. In this study, the STD data of different bands at each sampling point calculated in Section 3.2 is used as the uncertainty data caused by the spatial heterogeneity. Therefore, another set of interval soft data can be obtained as follows:

$$p_{ij} = R_{ij} - \omega_{ij}, \tag{23}$$

$$q_{ij} = R_{ij} + \omega_{ij}, \tag{24}$$

$$\chi_{soft_2} = \left\{ [\chi_{1j} \cdots \chi_{ij}]^T; \chi_{ij} \in [p_{ij}, q_{ij}], i = 1 \ldots 40, j = 1 \ldots 2151 \right\}. \tag{25}$$

Here, ω_j is the uncertainty data caused by the spatial heterogeneity; p_j and q_j are the possible lower and upper bounds of the second type soft data. Figure 4 shows the fluctuation range of spectral reflectance measured in situ that may be caused by spatial heterogeneity.

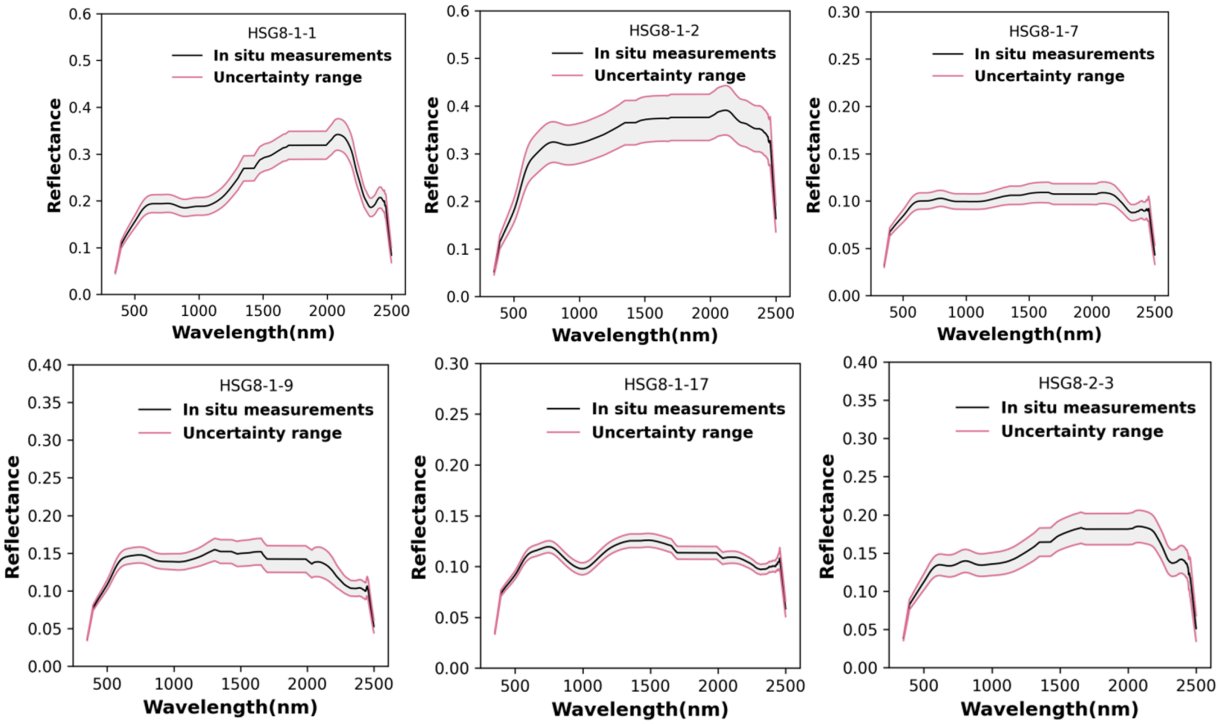

Figure 4. The fluctuation range in the in situ measured spectral reflectance of rocks caused by spatial heterogeneity at some sampling points.

3.4. Upscaling Results

As mentioned above, it is difficult to obtain the real spectral reflectance of the corresponding area at the pixel-scale. Since the spectra of 13 locations collected around each sampling point could cover at least the area of 3 m × 3 m (Figure 1), according to the evaluation results of spatial heterogeneity of 40 ground sampling points in Section 3.2, 10 sampling points with the smallest spatial heterogeneity are selected as ground verification points in this work. The arithmetic average of in situ measured spectral reflectance at 13 locations around the ground verification point is taken as the relative reference truth with 3 m spatial resolution, to evaluate the upscaling ability of the BME model.

Based on the spectral reflectance measured in situ, the spectral reflectance of rocks with 3 m spatial resolution are obtained by using the BME upscaling model. Figure 5 shows the scatter plot and its linear fitting results between the in situ measured and the upscaled spectral reflectance for the four typical absorption bands at 10 ground verification points. The red dots of different bands are concentrated near the 1:1 line, and the results of linear fitting almost coincide with the 1:1 line, which shows the outstanding upscaling ability. In addition, according to the linear fitting equation and R^2 given in Figure 5, the slope and R^2 are obviously closer to 1, which shows that the BME model can obtain ideal results at different bands.

In order to intuitively demonstrate the upscaling ability of the OK and the BME upscaling models. Figure 6 shows the comparison results between the in situ measured and the upscaled spectral reflectance at 6 ground verification points. Because most of the absorption characteristic of rocks are concentrated after 2000 nm, only the comparison results of spectral reflectance in the range of 2000 nm to 2500 nm are given in this work. In Figure 6, the upscaling results of the BME model at different verification points are obviously better. Both the spectral shape and reflectance are more consistent with the blue spectral representing the in situ measurements, and the spectral absorption characteristics

are better preserved. In comparison, the upscaling result of the OK model is significantly different from the blue spectral curve in spectral shape and reflectance, and there are some phenomena such as waveform deformation, absorption position shift, absorption characteristics disappearing and adding at some verification points.

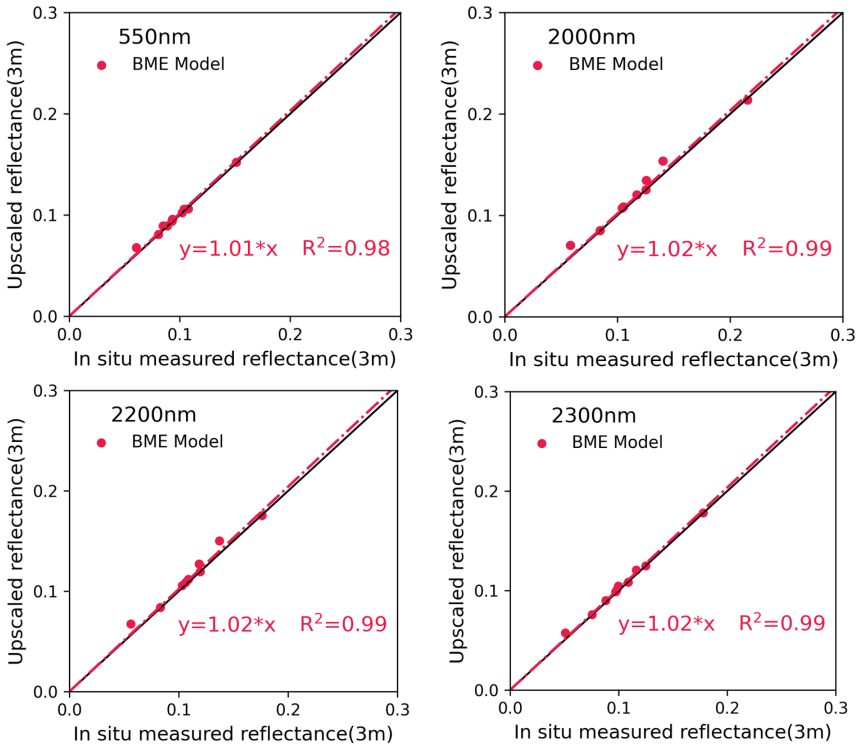

Figure 5. Scatter plots and linear fitting results of in situ measured and upscaled spectral reflectance at 10 ground validation points in the absorption bands. "*" for a multiplication sign.

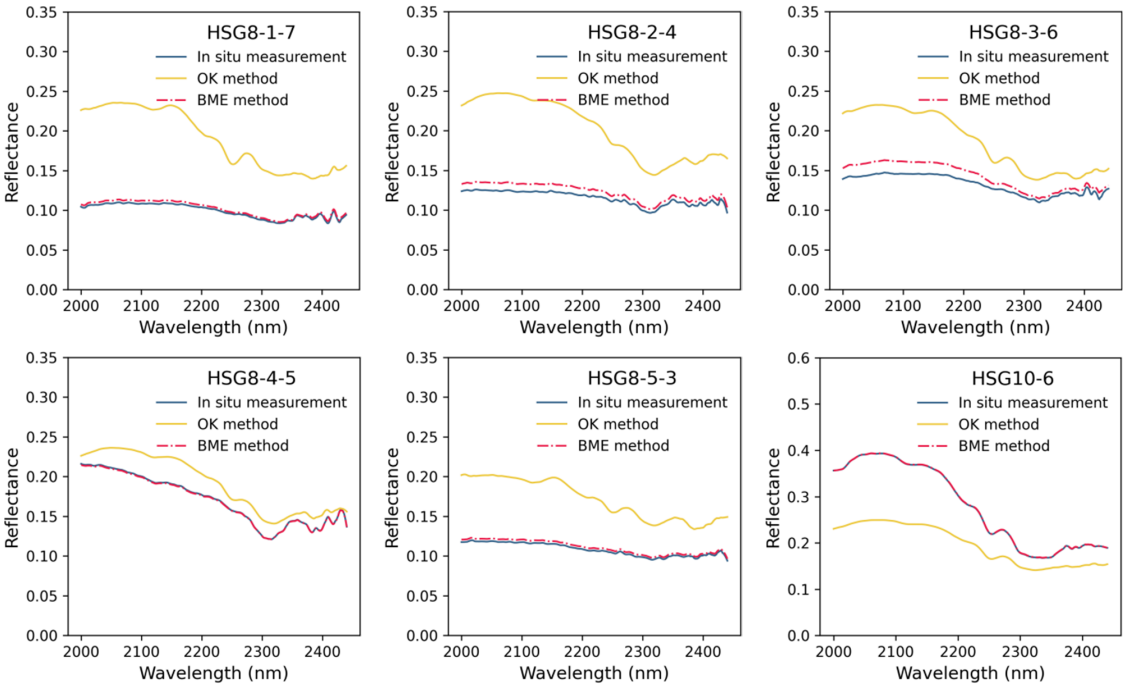

Figure 6. Comparison between the in situ measured spectral reflectance and the upscaled spectral reflectance with 3 m spatial resolution at 6 ground verification points.

3.5. Upscaling Model Evaluation

This section uses the LOO method to cross verify the upscaling ability of the Ordinary Least Squares (OLS), OK, and BME upscaling models. Table 2 contains the average calculation results of the evaluation indicators of the three models at 10 ground verification points. According to Table 2, the OLS model has the lowest upscaling ability, which shows the advantages of the OK and the BME model in introducing the spatial structure information of surface parameters into the upscaling process.

Table 2. The statistical results of accuracy evaluation indicators for three upscaling models.

Upscaling Models	MAE	RMSE	R^2	SAM
OLS model	0.043	0.056	−4.361	0.153
OK model	0.036	0.047	−4.828	0.148
BME model	0.005	0.006	0.978	0.009

In addition, the MAE, RMSE, and SAM of the BME model are much lower than those of the OK model, which proves that the BME model has stronger upscaling ability. In addition, the R^2 of the BME model is 0.978, which indicates that it has a better goodness of fit and can preserve the spectral characteristics of rocks to the maximum extent. However, the R^2 of the OK model is negative, which is mainly because the upscaling results of this model at some verification points are quite different from the in situ measured spectral reflectance, which proves that the BME model shows better stability.

The research results in Sections 3.4 and 3.5 show that the BME model has stronger upscaling ability and stability in terms of reflectance value, spectral shape, and absorption characteristics. This proves that introducing the uncertainty data caused by the inconsistency of SZA and SAA, as well as the uncertainty data caused by the spatial heterogeneity as soft data into the upscaling process can obtain better upscaling results. To sum up, the BME model can obtain ideal upscaling results, which can be used to quantitative study of spatial scale effect on rock spectral reflectance.

3.6. The Influence of Spatial Scale Effect

Table 3 summarizes the common spaceborne hyperspectral sensors launched and their spatial resolution [48]. As can be seen from Table 3, in recent years, the spatial resolutions of spaceborne hyperspectral sensors are concentrated at 10 m, 30 m, and 50 m. In addition, the spatial resolution of hyperspectral images obtained from the remote sensing flight test mostly range from one meter to several meters. Therefore, based on the BME upscaling model, the upscaled spectral reflectance of 40 ground sampling points with spatial resolutions of 1 m, 2 m, 3 m, 5 m, 10 m, 30 m, and 50 m are obtained. Then, the influence of spatial scale effect on the rock's spectra are analyzed using three aspects: the reflectance value, spectral shape, and diagnostic absorption characteristics.

Table 3. The common spaceborne hyperspectral sensors launched in recent years and their spatial resolution.

Sensor	Year	Country	Spatial Resolution
Aqua MODIS	1999	AMERICA	250 m, 500 m, 1000 m
EO-1 Hyperion	2000	AMERICA	30 m
PROBA CHRIS	2001	EUROPEAN SPACE AGENCY	17 m, 34 m
Terra MODIS	2002	AMERICA	250 m, 500 m, 1000 m
SZ-3 CMODIS	2002	CHINA	400–500 m
CE-1 IIM	2007	CHINA	200 m
HJ-1A HSI	2008	CHINA	100 m
FY-3 MERSI-1	2008	CHINA	250 m, 1000 m

Table 3. *Cont.*

Sensor	Year	Country	Spatial Resolution
TG-1 HSI	2011	CHINA	250 m, 500 m
SPARK HSI	2016	CHINA	50 m
GF5 AHSI	2018	CHINA	30 m
OHS HSI	2018	CHINA	10 m
ISS DESIS	2018	GERMANY	30 m
HySIS	2018	INDIA	30 m
ZY-1 02D AHSI	2019	CHINA	30 m
PRISMA	2019	ITALY	30 m
ALOS-3 HISUI	2020	JAPAN	30 m
EnMAP HSI	2020	GERMANY	30 m

3.6.1. Influence on Reflectance Value

Figure 7 compares the reflectance value of rock spectra with different spatial resolutions, in which the first row is the sampling point with the smallest ED in Table 1, and the second row is the largest ED. By comparison, the influence of spatial resolution changes on the reflectance value of rocks is closely related to the spatial heterogeneity of the sampling points. For the sampling points with small spatial heterogeneity and ED, the change in spatial resolution has little influence on the reflectance value, and the spectral curves under different spatial resolutions basically coincide. However, the change in spatial resolution has a great influence on the sampling points with large spatial heterogeneity, and the variation range of reflectance value may be greater than 0.2. Moreover, the difference in reflectance value between the in situ measured and the pixel-scale spectrum greater than 10 m spatial resolution is small, but when the spatial resolution is less than 10 m, the reflectance of the sampling points with large spatial heterogeneity begins to fluctuate greatly.

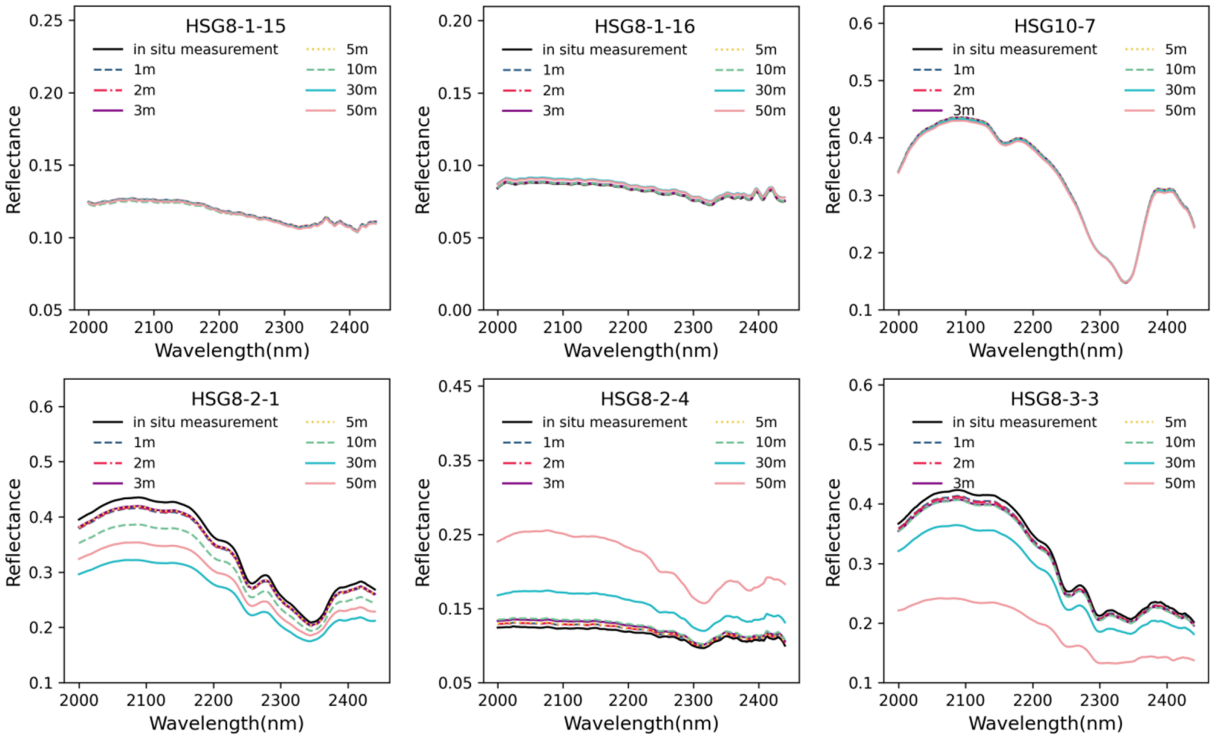

Figure 7. Comparison of the reflectance value of rock spectra with different spatial resolutions at some sampling points.

The ED is used to evaluate the difference in reflectance value caused by the change in spatial resolution. For the spectral reflectance measured in situ and the pixel-scale spectra with different spatial resolutions obtained by upscaling at the same sampling point, the ED between the two spectra was calculated, and the maximum ED was selected to evaluate the influence of spatial resolution on the reflectance at that sampling point. According to the statistical results of 40 sampling points, the ED between reflectance caused by the change in spatial resolution is between 0.056 and 6.271. Figure 8a displays the histogram of the maximum ED distribution of 40 sampling points. It can be seen that the influence of spatial resolution change has a large impact on the reflectance value at different sampling points. Nearly three quarters of the sampling points have a maximum ED of less than 2, and most of the sampling points have a maximum ED of less than 4, but a few sampling points exceed 4.

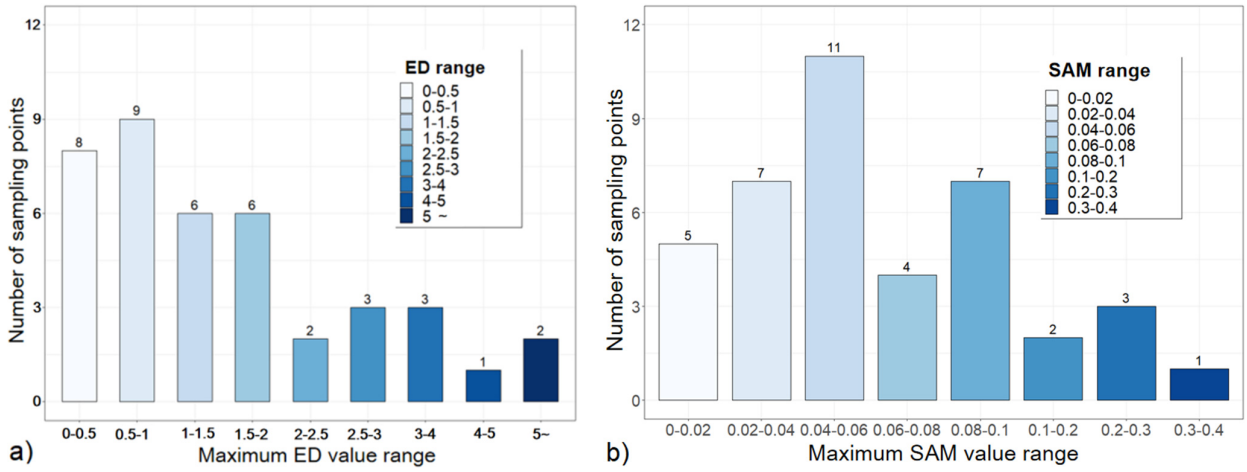

Figure 8. Histogram of maximum ED and maximum SAM distribution caused by spatial resolution change at 40 sampling points. (**a**) Maximum ED. (**b**) Maximum SAM.

3.6.2. Influence on Spectral Shape

The influence of spatial resolution change on the rock spectral shape at different sampling points is also quite different. Figure 9 presents a comparison chart of rock spectral shape with different spatial resolutions. The first row is the sampling points with smaller SAM in Table 1, the spectral shapes under different spatial resolutions are basically the same. However, for the three sampling points with largest SAM in the next row, the change in spatial scale has a great influence on the spectral shape. Taken together, the spectral shape between point-scale spectrum and the pixel-scale spectra with spatial resolution greater than 10 m have stronger similarity. However, there are significant differences in the shapes at the spatial resolution of 30 m and 50 m, and there are phenomena such as the waveform deformation, absorption position shift, and absorption characteristics disappearing and increasing.

SAM is used to evaluate the difference in spectral shape caused by the change in spatial resolution. Similarly, the SAM between the two spectra was calculated, and the maximum SAM was selected to evaluate the influence of spatial resolution on the spectral shape. The statistical results of 40 sampling points show that the SAM between rock spectra caused by the change in spatial resolution is between 0.005 and 0.370. From the histogram of the maximum SAM distribution shown in Figure 8b, it can be found that the maximum SAM distribution at different sampling points in the study area is dispersed. Among the 40 ground sampling points, the maximum SAM of most sampling points is less than 0.1, and a few sampling points are between 0.1 and 0.4.

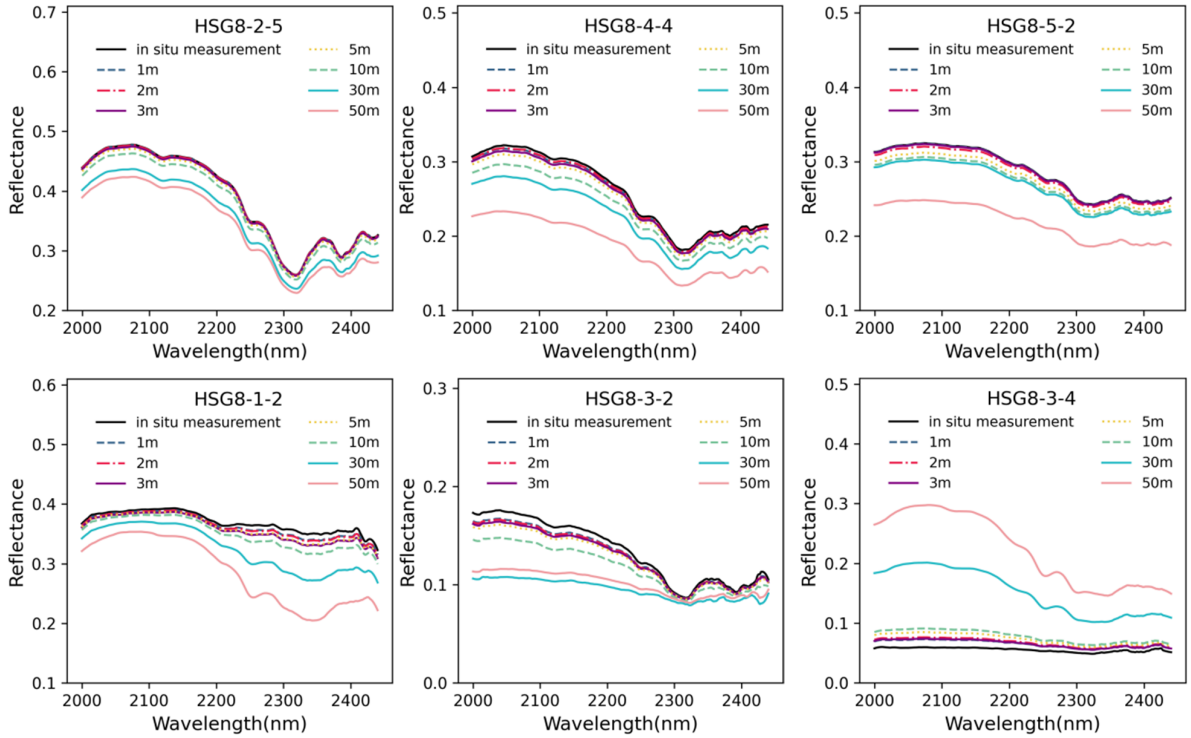

Figure 9. Comparison of the rock's spectral shape with different spatial resolutions at some sampling points.

3.6.3. Influence on Absorption Characteristics

In order to explore the influence of spatial resolution change on the spectral characteristic parameters of rocks, three sampling points with typical Chloritization absorption characteristics near 2250 nm are selected in this section. Figure 10 displays the variation trend and STD of 7 spectral characteristic parameters of 3 sampling points at 2250 nm with the decrease in spatial resolution.

An obvious phenomenon is that when the spatial resolution is greater than 10 m, the change in spatial resolution has little influence on the absorption position of rocks. When the spatial resolution is less than 10 m, the absorption position begins to drift slightly. For the absorption depth, absorption width, absorption area, and symmetry, the pixel-scale spectra with spatial resolution greater than 10 m have good consistency with the spectra measured in situ at this position, and the spectral characteristic parameters show an upward trend when the spatial resolution is less than 10 m. For the slope and spectral absorption, some sampling points show great irregular fluctuations; in particular, the slope showed positive and negative fluctuations. This may be influenced by the rock with different absorption characteristics nearby, which is related to the large spatial heterogeneity around the sampling point.

In order to explore the variation range of spatial scale effect on the diagnostic absorption characteristics, spectral characteristic parameters with different spatial resolutions at 2250 nm and 2350 nm were calculated for each point. The statistical results of the variation range of 7 spectral characteristic parameters of 40 sampling points are shown in Table 4. From the variation range, spectral absorption position, absorption depth, and spectral absorption index are less influenced by the change in spatial resolution. From the STD in Figure 10, the spectral absorption position and absorption depth are small. This result is consistent with the fact that the absorption position, absorption depth, and spectral absorption index of rocks diagnostic absorption characteristics are often used as the main criteria for distinguishing rock types.

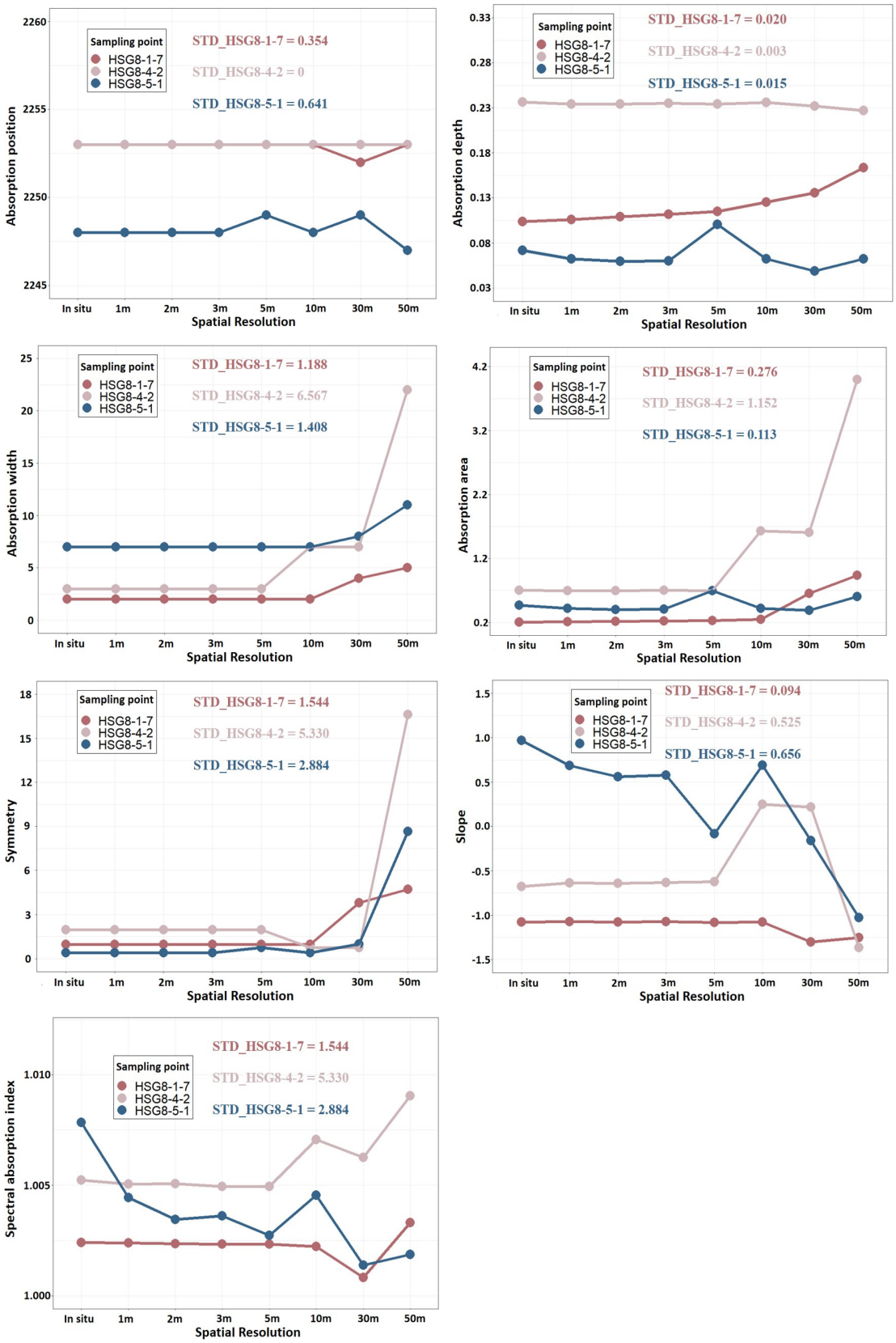

Figure 10. Trend diagram and STD of rock's spectral characteristic parameters at 2250 nm with the decrease in spatial resolution.

Table 4. Variation range of spectral characteristic parameters caused by the change in spatial resolution.

Spectral Characteristic Parameters	Variation Range (2250 nm)	Variation Range (2350 nm)
Absorption position (nm)	0–5	0–9
Absorption depth	0.004–0.468	0.007–0.490
Absorption width (nm)	0–21	0–23
Absorption area	0.081–4.276	0.037–6.401
Symmetry	0.009–15.327	0.0002–4.193
Slope	0.006–2.688	0.002–2.815
Spectral absorption index	0.001–0.115	0.0006–0.096

4. Discussion

4.1. Model Comparison

Among the three models, the OLS model has the weakest upscaling ability, which proves the advantages of the OK and the BME model in introducing the spatial structure information of surface parameters into the upscaling process. Compared with the OK model, the BME model shows better upscaling ability and stability. The main reason is that the OK model belongs to the optimal linear unbiased estimation, which is essentially a function of distance. Therefore, its upscaling results are more dependent on the spatial heterogeneity around the sampling point. For the sampling points with large spatial heterogeneity, it is difficult for the OK model to capture the spatial change, and the results are easily influenced by the other types of rocks. The BME upscaling model expands the ability to use measured data with uncertainty instead of a single observation value. And it obtains better upscaling results by incorporating multi-sourced data. As a spatial prediction technique, the BME model has been well applied in the related lithosphere field. At present, the BME model has obtained more accurate results than the OK model in predicting soil depth, soil water content, and soil respiration [30,49,50]. In addition, the BME model accurately describes the distribution of heavy metals in a lignite mining area in Greece [51]. This work proves the BME model can also obtain better results in spatial prediction and upscaling of rocks.

4.2. The Influence of Spatial Scale Effect

Experiments show that the influence of spatial scale effect on the reflectance value, spectral shape, and spectral characteristic parameters of rocks at different sampling points is quite different. This influence is closely related to the spatial heterogeneity of sampling points. The spectral absorption position, absorption depth, and spectral absorption index are less affected by spatial scale effect, which is more suitable for rock identification. For the Huangshan Copper–Nickel Ore District study area, the in situ measured spectrum at the sampling point with smaller spatial heterogeneity is in good agreement with the pixel-scale spectra with different spatial resolutions. For sampling points with large spatial heterogeneity, the pixel-scale spectra with spatial resolution greater than 10 m are in good agreement with the in situ measured spectrum at this position. However, when the spatial resolution is less than 10 m, there will be great differences in reflectance value, spectral shape, and characteristic parameters between the pixel-scale and the point-scale spectra, and the influence of spatial scale effect between the point-scale and the pixel-scale spectra should be considered in the subsequent application.

4.3. Comparison with Hymap Image

In this section, Hymap images of the study area collected by the Hymap airborne imaging spectrometer on 22 October 2002 are used to verify the ability of the upscaling model to reduce the influence of spatial scale effect. The band ranges of the image are from 450 nm to 2500 nm. The spectral resolution of visible-near-infrared (VNIR) is 15 nm, and for short-wave infrared (SWIR) is around 15 nm to 20 nm. This study area covers the images taken by the 19th and 20th flight path, therefore, the two Hymap images are

mosaic and cropped before preprocessing. The size of the image is 850 × 200 pixels, and the spatial resolution is 5 m, and the locations of 40 sampling points in the image are shown in Figure 1.

In the process of remote sensing imaging, the spectral detectability is easily influenced by sensor attitude, earth rotation, terrain fluctuation, local lighting, and atmospheric conditions, which leads to radiation error and geometric distortion in the image. Therefore, we carry out radiation correction on the raw Hymap image in the study area, with the aim of converting the Digital Number into the radiance data and eliminating the sensor error. Then, in order to eliminate geometric distortion and improve the accuracy of target location and recognition, this section carries out the geometric correction on the image. Subsequently, atmospheric correction is carried out to eliminate the influence of atmosphere and illumination on the reflection of ground objects and obtain the reflectance data. Finally, spectral resampling is performed on in situ measured and upscaled spectra to make them have the same spectral resolution as Hymap image. Because some bands cannot be used because of strong water vapor absorption, therefore, there are 122 bands after removing the water vapor absorption band.

For the preprocessed Hymap image, the quality of pixel data for some ground sampling points is not good, which is probably due to the performance of the instrument. In order to compare the reliability of the results, 20 ground sampling points with a good quality of image pixel were selected to verify the ability of the upscaling model to reduce the influence of spatial scale effect. Bar charts are used to compare the consistency between the upscaling results of two models and the Hymap data at the 5 m spatial resolution (Figure 11). Each sampling point in Figure 11 consists of two columns, representing the ratio of Hymap data to BME upscaling results and OK upscaling results, respectively. When the column approaches a straight line with $y = 1$, it indicates that the upscaling results are consistent with the Hymap data. According to Figure 11, it can be observed that compared with the OK upscaling results (red bars), the ratio of the Hymap data to BME upscaling results (yellow bars) was closer to 1 at almost sampling points. This shows that the reflectance of 5 m spatial resolution obtained based on the BME upscaling model is more consistent with the Hymap data. The BME upscaling model effectively reduces the local influence of spatial scale effect and shows stronger upscaling ability.

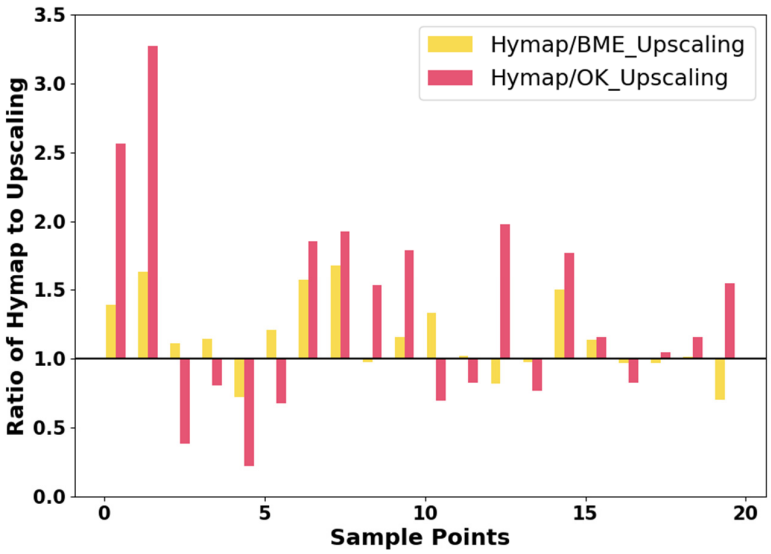

Figure 11. Comparison of the ratios of Hymap data and upscaling results at 20 sampling points.

4.4. Popularization and Application

Based on the above research, this paper puts forward a set of processes and steps to realize the upscaling of rock spectral reflectance and evaluate the influence of the spatial scale effect in the study area. Through this process, the BME upscaling model established

in this work can be generalized to geological applications in other areas. First of all, it is necessary to collect the spectral reflectance of objects as evenly and widely as possible around the ground sampling point to evaluate the spatial heterogeneity of the sampling point. For sampling points with small spatial heterogeneity, the arithmetic average of ground multi-point measurement spectra can be directly used to replace the pixel-scale spectra with different spatial resolutions. When the spatial heterogeneity of sampling points is large, it is necessary to upscale the ground measurement spectrum to the pixel-scale spectrum with the same spatial resolution as the remote sensing image before it can be applied. Before upscaling, it is necessary to quantitatively evaluate the spatial autocorrelation of the study area. For the study area with strong spatial autocorrelation, the BME model based on geostatistics can obtain better upscaling results. However, for the area without spatial autocorrelation, arithmetic average and empirical regression methods are more suitable to realize upscaling.

5. Conclusions

The huge spatial heterogeneity of the land surface and the limited footprint coverage make the spectral reflectance of in situ measurements unable to represent the remote sensing products. Based on the advantage of the BME method, the uncertainty data caused by the difference in SZA, SAA, and spatial heterogeneity were introduced into the BME method in this work. The BME upscaling model is compared with the OK and the OLS model to verify the advantages of introducing soft data. Then, based on the BME model and in situ measurements data, the spectral reflectance of rocks is upscaled from the point-scale to meter-scale and 10 m-scale. Finally, the influence of spatial scale effect on the reflectance value, spectral shape and absorption characteristics is quantitatively evaluated.

The experimental results show that the OLS model has lower upscaling ability than the OK and the BME model. Compared with the traditional OK model which only uses hard data, the MAE, RMSE, and SAM of the BME model are improved by 0.031, 0.041, and 0.139, respectively, and R^2 can reach to 0.978. This work proves that the accuracy of upscaling results can be improved by introducing the spatial structure information of surface parameters into the upscaling process. In addition, the BME model shows great advantages in estimating the reflectance values, spectral shapes, and spectral absorption characteristics of rocks after introducing uncertainty data as soft data. The introduced soft data can provide effective spatial information for spatial estimation and prediction.

The upscaling results of the Huangshan Copper–Nickel Ore District study area show that the maximum ED of rock spectral fluctuation caused by spatial resolution change is basically between 0 and 4, and the maximum ED can reach 6.271. The maximum SAM is basically between 0 and 0.1, which can reach 0.370. Due to the spatial scale effect, the variation range of spectral absorption position, absorption depth, and spectral absorption index of rocks is small, which is more suitable as the main basis for distinguishing rock types. In addition, for the area with similar spatial heterogeneity to the Huangshan Copper–Nickel Ore District study area. This study believes that the spatial scale effect has little influence on the remote sensing image with spatial resolution greater than 10 m and the in situ measurement spectrum. In rock-related applications, when the spatial resolution of the image is less than 10 m, it is necessary to upscale the in situ measurement spectrum to the corresponding pixel-scale.

This study proves that introducing uncertain data into the BME upscaling model as soft data can achieve ideal upscaling results. However, this study only focused on the uncertainty caused by the differences in SZA, SAA, and spatial heterogeneity. In fact, there are many reasons for the spatial scale effect between point-scale spectrum and the pixel-scale spectrum. Moreover, a large number of previously accumulated data, expert knowledge, and existing mineral identification and classification results also can be introduced into the BME upscaling method as soft data. Therefore, further research about how to introduce the above useful knowledge into the BME model in the form of appropriate soft data representation to establish a better BME model will be a fruitful

field. In addition, this study takes the Huangshan Copper–Nickel Ore District as the study area to explore the influence of spatial scale effect on rock spectra. The universality of the conclusions in this paper for other regions will be our future research direction.

Author Contributions: Conceptualization, Z.W., G.J. and H.Z.; methodology, Z.W. and G.J.; writing—original Draft, Z.W.; writing—review and editing, G.J.; data curation, Z.W.; investigation, F.W.; visualization, Z.W. and F.W. All authors have read and agreed to the published version of the manuscript.

Funding: This research received no external funding.

Data Availability Statement: The original contributions presented in the study are included in the article, further inquiries can be directed to the corresponding author.

Conflicts of Interest: The authors declare that they have no known competing financial interests or personal relationships that could have appeared to influence the work reported in this paper.

References

1. Brown, L.A.; Camacho, F.; García-Santos, V.; Origo, N.; Fuster, B.; Morris, H.; Pastor-Guzman, J.; Sánchez-Zapero, J.; Morrone, R.; Ryder, J.; et al. Fiducial reference measurements for vegetation bio-geophysical variables: An end-to-end uncertainty evaluation framework. *Remote Sens.* **2021**, *13*, 3194. [CrossRef]
2. Buman, B.; Hueni, A.; Colombo, R.; Cogliati, S.; Celesti, M.; Julitta, T.; Burkart, A.; Siegmann, B.; Rascher, U.; Drusch, M.; et al. Towards consistent assessments of in situ radiometric measurements for the validation of fluorescence satellite missions. *Remote Sens. Environ.* **2022**, *274*, 112984. [CrossRef]
3. Fowler, J.; Waldner, F.; Hochman, Z. All pixels are useful, but some are more useful: Efficient in situ data collection for crop-type mapping using sequential exploration methods. *Int. J. Appl. Earth Obs. Geoinf.* **2020**, *91*, 102114. [CrossRef]
4. Hadley, B.C.; Garcia-Quijano, M.; Jensen, J.R.; Tullis, J.A. Empirical versus model-based atmospheric correction of digital airborne imaging spectrometer hyperspectral data. *Geocarto Int.* **2005**, *20*, 21–28. [CrossRef]
5. Wang, Y.W.; Leng, P.; Peng, J.; Marzahn, P.; Ludwig, R. Global assessments of two blended microwave soil moisture products CCI and SMOPS with in-situ measurements and reanalysis data. *Int. J. Appl. Earth Obs. Geoinf.* **2021**, *94*, 102234. [CrossRef]
6. Wu, X.D.; Wen, J.G.; Xiao, Q.; Liu, Q.; Peng, J.J.; Dou, B.C.; Li, X.H.; You, D.Q.; Tang, Y.; Liu, Q.H. Coarse scale in situ albedo observations over heterogeneous snow-free land surfaces and validation strategy: A case of MODIS albedo products preliminary validation over northern China. *Remote Sens. Environ.* **2016**, *184*, 25–39. [CrossRef]
7. Song, G.Q.; Wang, J.; Zhao, Y.Y.; Yang, D.D.; Lee, C.K.F.; Guo, Z.F.; Detto, M.; Alberton, B.; Morellato, P.; Nelsom, B.; et al. Scale matters: Spatial resolution impacts tropical leaf phenology characterized by multi-source satellite remote sensing with an ecological-constrained deep learning model. *Remote Sens. Environ.* **2024**, *304*, 114027. [CrossRef]
8. Qin, J.; Yang, K.; Lu, N.; Chen, Y.Y.; Zhao, L.; Han, M.L. Spatial upscaling of in-situ soil moisture measurements based on MODIS-derived apparent thermal inertia. *Remote Sens. Environ.* **2013**, *138*, 1–9. [CrossRef]
9. Marceau, D.J. The scale issue in the social and natural sciences. *Can. J. Remote Sens.* **1999**, *25*, 347–356. [CrossRef]
10. Wen, J.G.; Liu, Q.; Liu, Q.H.; Xiao, Q.; Li, X.W. Scale effect and scale correction of land-surface albedo in rugged terrain. *Int. J. Remote Sens.* **2009**, *30*, 5397–5420. [CrossRef]
11. Cerdan, O.; Le Bissonnais, Y.; Govers, G.; Lecomte, V.; Van Oost, K.; Couturier, A.; King, C.; Dubreuil, N. Scale effect on runoff from experimental plots to catchments in agricultural areas in Normandy. *J. Hydrol.* **2004**, *299*, 4–14. [CrossRef]
12. Wu, X.D.; Xiao, Q.; Wen, J.G.; You, D.Q.; Hueni, A. Advances in quantitative remote sensing product validation: Overview and current status. *Earth-Sci. Rev.* **2019**, *196*, 102875. [CrossRef]
13. Wu, H.; Li, Z.L. Scale issues in remote sensing: A review on analysis, processing and modeling. *Sensors* **2009**, *9*, 1768–1793. [CrossRef] [PubMed]
14. Hu, Z.L.; Islam, S. Effects of spatial variability on the scaling of land surface parameterizations. *Bound.-Layer Meteorol.* **1997**, *83*, 441–461. [CrossRef]
15. Wu, H.; Tang, B.H.; Li, Z.L. Impact of nonlinearity and discontinuity on the spatial scaling effects of the leaf area index retrieved from remotely sensed data. *Int. J. Remote Sens.* **2013**, *34*, 3503–3519. [CrossRef]
16. Román, M.O.; Schaaf, C.B.; Lewis, P.; Gao, F.; Anderson, G.P.; Privette, J.L.; Strahler, A.H.; Woodcock, C.E.; Barnsley, M. Assessing the coupling between surface albedo derived from MODIS and the fraction of diffuse skylight over spatially-characterized landscapes. *Remote Sens. Environ.* **2010**, *114*, 738–760. [CrossRef]
17. Wang, Z.S.; Schaaf, C.B.; Strahler, A.H.; Chopping, M.J.; Román, M.O.; Shuai, Y.M.; Woodcock, C.E.; Hollinger, D.Y.; Fitzjarrald, D.R. Evaluation of MODIS albedo product (MCD43A) over grassland, agriculture and forest surface types during dormant and snow-covered periods. *Remote Sens. Environ.* **2014**, *140*, 60–77. [CrossRef]
18. Origo, N.; Gorroño, J.; Ryder, J.; Nighttingale, J.; Bialek, A. Fiducial Reference Measurements for validation of Sentinel-2 and Proba-V surface reflectance products. *Remote Sens. Environ.* **2020**, *241*, 111690. [CrossRef]

19. Pflug, B.; Louis, J.; de los Reyes, R.; Pflug, K.; Mueller-Wilm, U.; Quang, C.; Quirino Iannone, R.; Reinartz, P. Evaluation of SEN2COR surface reflectance products over land surface with reference measurements on ground. In Proceedings of the IGARSS 2022—2022 IEEE International Geoscience and Remote Sensing Symposium, Kuala Lumpur, Malaysia, 17–22 July 2022; pp. 4308–4311. [CrossRef]
20. Riihelä, A.; Laine, V.; Manninen, T.; Palo, T.; Vihma, T. Validation of the Climate-SAF surface broadband albedo product: Comparisons with in situ observations over Greenland and the ice-covered Arctic Ocean. *Remote Sens. Environ.* **2010**, *114*, 2779–2790. [CrossRef]
21. Shi, Y.C.; Wang, J.D.; Qin, J.; Qu, Y.H. An Upscaling Algorithm to Obtain the Representative Ground Truth of LAI Time Series in Heterogeneous Land Surface. *Remote Sens.* **2015**, *7*, 12887–12908. [CrossRef]
22. Cohen, W.B.; Maiersperger, T.K.; Gower, S.T.; Turner, D.P. An improved strategy for regression of biophysical variables and Landsat ETM+ data. *Remote Sens. Environ.* **2003**, *84*, 561–571. [CrossRef]
23. Crow, W.T.; Ryu, D.; Famiglietti, J.S. Upscaling of field-scale soil moisture measurements using distributed land surface modeling. *Adv. Water Resour.* **2005**, *28*, 1–14. [CrossRef]
24. Kang, J.; Jin, R.; Li, X.; Zhang, Y. Block kriging with measurement errors: A case study of the spatial prediction of soil moisture in the middle reaches of Heihe River Basin. *IEEE Geosci. Remote Sens. Lett.* **2016**, *14*, 87–91. [CrossRef]
25. Wang, J.; Ge, Y.; Heuvelink, G.B.M.; Zhou, C. Upscaling In Situ Soil Moisture Observations to Pixel Averages with Spatio-Temporal Geostatistics. *Remote Sens.* **2015**, *7*, 11372–11388. [CrossRef]
26. Kang, J.; Jin, R.; Li, X. Regression kriging-based upscaling of soil moisture measurements from a wireless sensor network and multiresource remote sensing information over heterogeneous cropland. *IEEE Geosci. Remote Sens. Lett.* **2014**, *12*, 92–96. [CrossRef]
27. Christakos, G. A Bayesian/maximum-entropy view to the spatial estimation problem. *Math. Geol.* **1990**, *22*, 763–777. [CrossRef]
28. Christakos, G.; Li, X.Y. Bayesian maximum entropy analysis and map: A farewell to kriging estimators? *Math. Geol.* **1998**, *30*, 435–462. [CrossRef]
29. Yu, H.L.; Chen, J.C.; Christakos, G.; Jerrett, M. BME estimation of residential exposure to ambient PM10 and ozone at multiple time scales. *Environ. Health Perspect.* **2009**, *117*, 537–544. [CrossRef]
30. Gao, S.G.; Zhu, Z.L.; Liu, S.M.; Jin, R.; Yang, G.C.; Tan, L. Estimating the spatial distribution of soil moisture based on Bayesian maximum entropy method with auxiliary data from remote sensing. *Int. J. Appl. Earth Obs. Geoinf.* **2014**, *32*, 54–66. [CrossRef]
31. Li, A.H.; Bo, Y.C.; Chen, L. Bayesian maximum entropy data fusion of field-observed leaf area index (LAI) and Landsat Enhanced Thematic Mapper Plus-derived LAI. *Int. J. Remote Sens.* **2013**, *34*, 227–246. [CrossRef]
32. Fan, L.; Xiao, Q.; Wen, J.G.; Liu, Q.; Jin, R.; You, D.Q.; Li, X.W. Mapping High-Resolution Soil Moisture over Heterogeneous Cropland Using Multi-Resource Remote Sensing and Ground Observations. *Remote Sens.* **2015**, *7*, 13273–13297. [CrossRef]
33. Murphy, R.J.; Monteiro, S.T.; Schneider, S. Evaluating classification techniques for mapping vertical geology using field-based hyperspectral sensors. *IEEE Trans. Geosci. Remote Sens.* **2012**, *50*, 3066–3080. [CrossRef]
34. Dong, X.F.; Gan, F.P.; Li, N.; Yan, B.K.; Zhang, L.; Zhao, J.Q.; Yu, J.C.; Liu, R.Y.; Ma, Y.N. Fine mineral identification of GF-5 hyperspectral image. *Natl. Remote Sens. Bull.* **2020**, *24*, 454–464. [CrossRef]
35. Li, G.J.; Yang, X.S.; Zhang, X.; Li, X.M.; Li, D.N.; Du, C. Application and analysis of ZY1-02D hyperspectral data in geological and mineral survey. *Remote Sens. Nat. Resour.* **2021**, *33*, 134. [CrossRef]
36. Li, Y.; Zhang, Y.; Hu, L.Q.; Lu, Q.F.; Lu, N.M. Investigation of optical environment changes in the Dunhuang gobi site of the Chinese radiometric calibration sites. *Chin. Opt.* **2021**, *14*, 1231–1242. [CrossRef]
37. Kodikara, G.R.L.; Woldai, T.; van Ruitenbeek, F.J.A.; Kuria, Z.; van der Meer, F.; Shepherd, K.D.; van Hummel, G.J. Hyperspectral remote sensing of evaporate minerals and associated sediments in Lake Magadi area, Kenya. *Int. J. Appl. Earth Obs. Geoinf.* **2012**, *14*, 22–32. [CrossRef]
38. Vishnu, S.; Nidamanuri, R.R.; Bremananth, R. Spectral material mapping using hyperspectral imagery: A review of spectral matching and library search methods. *Geocarto Int.* **2013**, *28*, 171–190. [CrossRef]
39. Zhang, Z.J.; Gan, F.P.; Li, X.Q.; Xu, Y.F.; Liang, S.N. The Extraction of Altered Mineral Information Based on ASTER Data:A Case Study of the Huangshan Copper- Nickel Ore District in Hami. *Remote Sens. Nat. Resour.* **2012**, *2*, 85–91. [CrossRef]
40. ASD. *ASD Technical Guide*, 3rd ed.; Analytical Spectral Devices CO., Inc.: Boulder, CO, USA, 1999; pp. 1–140. Available online: https://gep.uchile.cl/Biblioteca/radiometr%C3%ADa%20de%20campo/TechGuide.pdf (accessed on 28 May 2024).
41. He, J.Y.; Kolovos, A. Bayesian maximum entropy approach and its applications: A review. *Stoch. Environ. Res. Risk Assess.* **2018**, *32*, 859–877. [CrossRef]
42. Kruse, F.A.; Boardman, J.W.; Lefkoff, A.B.; Young, J.M.; Kierein-Young, K.S.; Cocks, T.D.; Jensen, R.; Cocks, P.A. HyMap: An Australian hyperspectral sensor solving global problems-results from USA HyMap data acquisitions. In Proceedings of the 10th Australasian Remote Sensing and Photogrammetry Conference, Adelaide, Australia, 21–25 August 2000; pp. 18–23. Available online: https://www.ugpti.org/smartse/research/citations/downloads/Cocks-More_about_HyMAP-1998.pdf (accessed on 6 August 2024).
43. Christakos, G.; Serre, M.L.; Kovitz, J.L. BME representation of particulate matter distributions in the state of California on the basis of uncertain measurements. *J. Geophys. Res. Atmos.* **2001**, *106*, 9717–9731. [CrossRef]
44. Douaik, A.; Van Meirvenne, M.; Tóth, T. Soil salinity mapping using spatio-temporal kriging and Bayesian maximum entropy with interval soft data. *Geoderma* **2005**, *128*, 234–248. [CrossRef]
45. Lee, Y.M.; Ellis, J.H. On the equivalence of kriging and maximum entropy estimators. *Math. Geol.* **1997**, *29*, 131–152. [CrossRef]

46. Kruse, F.A.; Lefkoff, A.B.; Boardman, J.W.; Heidebrecht, K.B.; Shapiro, A.T.; Barloon, P.J.; Goetz, A.F.H. The spectral image processing system (SIPS)—Interactive visualization and analysis of imaging spectrometer data. *Remote Sens. Environ.* **1993**, *44*, 145–163. [CrossRef]
47. Zhao, H.J.; Wang, Z.W.; Jia, G.R.; Tian, J.; Jin, S.L.; Liang, S.N.; Liu, Y.M. The Impact and Correction of Sensitive Environmental Factors on Spectral Reflectance Measured In Situ. *Remote Sens.* **2023**, *15*, 5332. [CrossRef]
48. Zhong, Y.F.; Wang, X.Y.; Wang, S.Y.; Zhang, L.P. Advances in spaceborne hyperspectral remote sensing in China. *Geo-Spat. Inf. Sci.* **2021**, *24*, 95–120. [CrossRef]
49. Orton, T.G.; Lark, R.M. Estimating the local mean for Bayesian maximum entropy by generalized least squares and maximum likelihood, and an application to the spatial analysis of a censored soil variable. *Eur. J. Soil Sci.* **2007**, *58*, 60–73. [CrossRef]
50. Hu, J.G.; Zhou, J.; Zhou, G.M.; Luo, Y.Q.; Xu, X.J.; Li, P.H.; Liang, J.Y. Improving estimations of spatial distribution of soil respiration using the Bayesian maximum entropy algorithm and soil temperature as auxiliary data. *PLoS ONE* **2016**, *11*, e0146589. [CrossRef]
51. Modis, K.; Vatalis, K.I.; Sachanidis, C. Spatiotemporal risk assessment of soil pollution in a lignite mining region using a Bayesian maximum entropy (BME) approach. *Int. J. Coal Geol.* **2013**, *112*, 173–179. [CrossRef]

Disclaimer/Publisher's Note: The statements, opinions and data contained in all publications are solely those of the individual author(s) and contributor(s) and not of MDPI and/or the editor(s). MDPI and/or the editor(s) disclaim responsibility for any injury to people or property resulting from any ideas, methods, instructions or products referred to in the content.